The Dynamics of Northwest Summer Winds over the Santa Barbara Channel

ERIC D. SKYLLINGSTAD AND PHILIP BARBOUR

College of Oceanic and Atmospheric Sciences, Oregon State University, Corvallis, Oregon

CLIVE E. DORMAN

Center for Coastal Studies, Scripps Institute of Oceanography, San Diego, California

(Manuscript received 21 March 2000, in final form 18 August 2000)

ABSTRACT

A mesoscale model is used to examine the dynamics of northwest flow over the Santa Barbara Channel region. Three cases are considered, each characterized by typical summertime synoptic conditions, but with differences in pressure gradient strength and marine boundary layer depth (MBL). The first case examines a relatively deep MBL and strong pressure gradient. Case 2 is characterized by a more shallow MBL and weaker pressure gradient, and case 3 represents a transition from a deep MBL to shallow conditions. In all cases, simulated surface winds show reasonable agreement with observations over most of the model domain, with the exception of regions near abrupt terrain changes.

Results from the model indicate that the flow with a deep MBL (~400 m) and strong pressure gradient (case 1) is supercritical, causing regions of acceleration and expansion in the lee of Point Conception. When the MBL is shallow (~150 m) (case 2), a transcritical flow scenario exists with subcritical flow upstream from Point Conception and a supercritical flow region over the Santa Barbara Channel and downstream from the Channel Islands. Flow over the channel is strongly affected by diurnal heating in shallow MBL cases, reversing direction in step with a land breeze circulation induced by nighttime cooling. The land breeze forces an internal wave disturbance that propagates westward across the channel, eliminating the supercritical flow region in the lee of Point Conception. Conditions with a deep MBL (~400 m) produce less variability in the surface winds, except for the region sheltered by the Santa Ynez Mountains. An expansion fan is still evident in this case, but it is produced by the interaction of the flow with higher terrain north and east of the channel. The low hills on Point Conception and the Channel Islands do not have a large blocking effect on the surface flow when the MBL is deep.

Analysis of the momentum budget supports the conclusion that the boundary layer behaves like a transcritical hydraulic flow when the MBL is shallow. Except for the open ocean region, the Coriolis term is minor in comparison with the pressure and advection terms. Diurnal heating effects are evident in the nearshore pressure term, which varies from offshore during the late evening to onshore in the afternoon. These effects are most significant when the MBL is shallow and can augment the hydraulically forced pressure pattern, causing a stronger expansion fan in the late afternoon and a collapse of the expansion fan during the early morning.

1. Introduction

Wind fields along the west coast of North America are strongly influenced by the interaction of the marine boundary layer (MBL) with coastal topography, and by the sea breeze circulation generated by differential surface heating. During the summer, these interactions are particularly important over southern California extending from Point Conception in the north to the Baja peninsula along the coast of Mexico. Summer synoptic conditions along the west coast are characterized by a persistent synoptic high pressure over the Pacific Ocean coupled with interior low pressure generated by surface solar heating (Dorman and Winant 1995, 2000; Dorman et al. 2000). Enhanced northerly winds are generated along the coast as the MBL is blocked by the coastal mountain ranges. Wind perturbations forced by coastal features such as points and variations in the coastal topography are affected by heating, forming circulations with a strong diurnal pattern. Perhaps the largest of these circulations is produced by Point Conception (PC) and the Santa Ynez Mountains, which amount to a nearly 90° change in the coast orientation and a significant blocking feature to the northerly flow (Fig. 1a). The abrupt change in the coastline at Point Conception often causes summer winds over the Santa Barbara Channel (SBC) to decrease dramatically from strong northwesterly winds at the western end of the channel to light westerly wind conditions in the east.

Corresponding author address: Dr. Eric Skyllingstad, College of Oceanic and Atmospheric Sciences, 104 Ocean Administration Building, Oregon State University, Corvallis, OR 97331-5503.
E-mail: skylling@oce.orst.edu

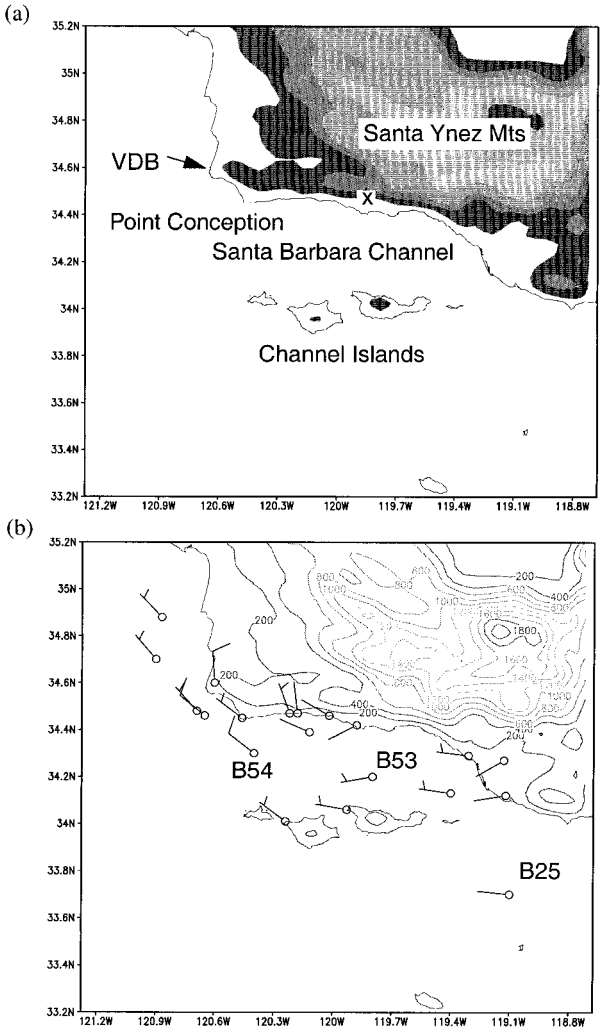

FIG. 1. (a) Geographical landmarks in the SBC region and (b) average wind vectors from May–Jul 1996 (taken from Dorman and Winant 2000). Also labeled are buoys 25, 53, and 54, and Vandenburg Air Force base (VDB). Terrain height is in m. Wind barbs throughout figures are full wind barb 10 m s^{-1}, half wind barb 5 m s^{-1}. The × in (a) is the approximate location of the Goleta profiler.

Climatological analysis by Dorman and Winant (2000) and Dorman et al. (2000) show how PC dominates the average summer wind fields over the SBC (Fig. 1b). As the northwesterly flow rounds the point, wind speeds typically increase from ~5 m s^{-1} north of the point to ~10 m s^{-1} at the western end of the SBC. The wind increase extends to about the middle of the channel, where the wind speed falls rapidly to ~3 m s^{-1} and backs to a more westerly direction. The wind field pattern is modulated by daytime diurnal heating, causing an increase in the wind speeds in the afternoon (Caldwell et al. 1986; Dorman and Winant 2000) as shown by conditional averages (Fig. 2). Relaxation of the synoptic pressure gradient with traveling synoptic disturbances causes a large change in the winds over the SBC and a reduction in the coherent structure and diurnal effects shown in Fig. 2. The approach of a trough often causes a cyclonic mesoscale eddy that covers the Southern California Bight. This ''Catalina eddy'' has a low center near Catalina Island causing increased stratus cloud cover and higher inversion base heights. Eddy events typically last for 2–3 days and may occur twice in a single-month period. Since the appearance of the earliest published reference (Rosenthal 1968), there has been periodic discussion concerning the dynamics of Catalina eddy events (Bosart 1983; Dorman, 1985; Wakimoto 1987; Mass and Albright 1989; Clark and Dembeck 1991). Our focus in this paper does not include Catalina eddy events but centers on the more common northwest summer flow pattern.

As Fig. 2 shows, a significant feature of the wind fields over the SBC is the substantial horizontal and temporal variability in the wind direction and speed. One consequence of this variability is a strong response in the ocean circulation, which is greatly affected by changes in the location and strength of the atmospheric boundary layer flow around PC. Field experiments show that north of PC the water mass characteristics follow classic upwelling conditions (Brink 1983; Huyer 1983; Atkinson et al. 1986). Inside the SBC, however, the circulation exhibits a complex behavior with an overall cyclonic circulation dependent on the surface wind stress and the ocean pressure gradient (Harms and Winant 1998). With northwest winds, the channel circulation generally follows a counterclockwise direction, with inflow just north of the Channel Islands and a return flow along the coast. This pattern breaks down when wind conditions change, implying that the large horizontal variation of the surface winds has a primary role in forcing the flow. Understanding what controls the wind fields is therefore essential for predicting the ocean circulation in the SBC.

Flow features around points and capes are often described using hydraulic theory for wall-bounded channel flow (Winant et al. 1988; Samelson 1992; Rogerson, 1999; Dorman et al. 1999). For example, the flow around PC can be conceptually modeled as a single layer fluid forced along the coast by the synoptic-scale pressure pattern. As the MBL moves along the coastline, the flow accelerates and decelerates in response to restrictions generated by the coastal topography. If the MBL is capped by a well-defined stable layer or inversion, the behavior of the flow can be described using a Froude number, $\mathrm{Fr} = U/(Nh)$, where U is the average wind speed in the MBL, $N = (g/\theta)\partial\theta/\partial z$, is the Brunt–Väisälä frequency of the inversion layer above the MBL, θ is the potential temperature, g is gravity, and h is the MBL depth. Here, Fr is roughly equivalent to the ratio of the flow kinetic energy to the potential energy produced by perturbations in the depth of the MBL. For flow around coastal points conditions are said to be supercritical when the upstream $\mathrm{Fr} > 1$, subcritical when $\mathrm{Fr} < 1$, and transcritical when $1 > \mathrm{Fr} > 0.5$. These designations refer to the maximum speed of propagation

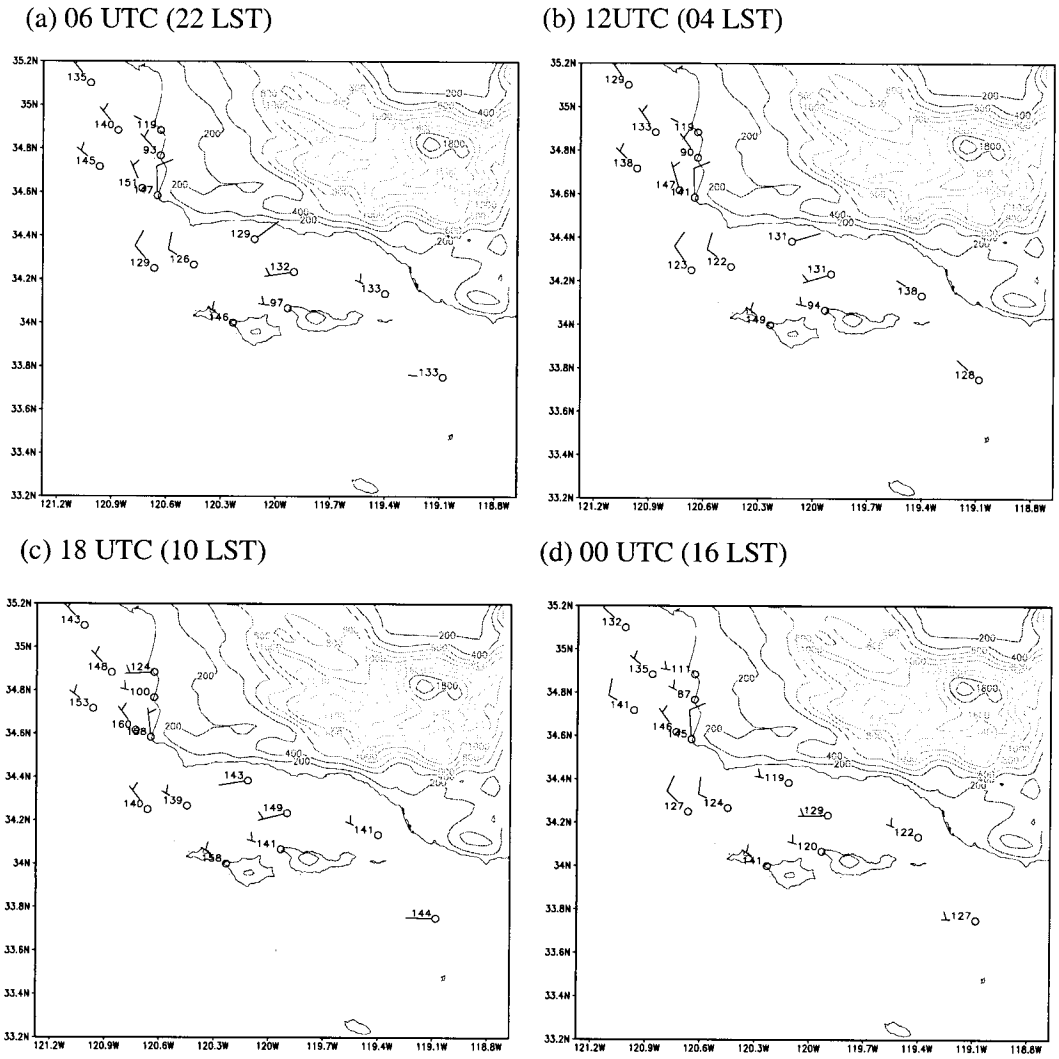

FIG. 2. Conditionally averaged winds from May–Sep 1998 for (a) 0600, (b) 1200, (c) 1800, and (d) 0000 UTC. Wind fields were averaged only for times when the wind direction at buoy 54 was between 285° and 345°.

for gravity waves contained in the MBL. For subcritical flow, gravity wave disturbances propagate faster than the background velocity and can move upstream from coastal features. In contrast, disturbances cannot move upstream in supercritical flow because the average flow velocity exceeds the maximum possible internal gravity wave speed.

Restrictions and expansions in the flow created by headlands cause Fr to vary depending on the MBL depth, velocity, and stability. If the marine layer flow is supercritical (Samelson 1992) or transcritical (Rogerson 1999) next to a topographical feature, then an expansion fan will form in the immediate lee of the coastal point where the MBL thins and accelerates. These two flow behaviors are shown schematically in Fig. 3 for the flow around PC. For supercritical conditions, the flow is relatively smooth with an acceleration in passing PC and a deceleration east and south of the SBC region. Transcritical flow shows a similar behavior, but with a more significant jump in velocity over the western SBC and corresponding drop in velocity east of the region. Dorman and Winant (2000) apply hydraulic theory to explain the turning of the winds in the western SBC as the flow rounds PC as shown in Fig. 3. Their analysis emphasizes that the pressure gradient and flow speed near the western end of the SBC support the existence of supercritical or transcritical flow. What is not determined are the effects of diurnal heating on the SBC circulation and if flow transitions can be forced by the local sea breeze circulations. For example, Rogerson (1999) demonstrates that in transcritical cases, perturbations of the subcritical flow region south of coastal points can set up a trapped disturbance that propagates upstream, gradually decreasing the area of supercritical flow. Applied to the SBC problem (Fig. 3b), a disturbance created in the eastern SBC

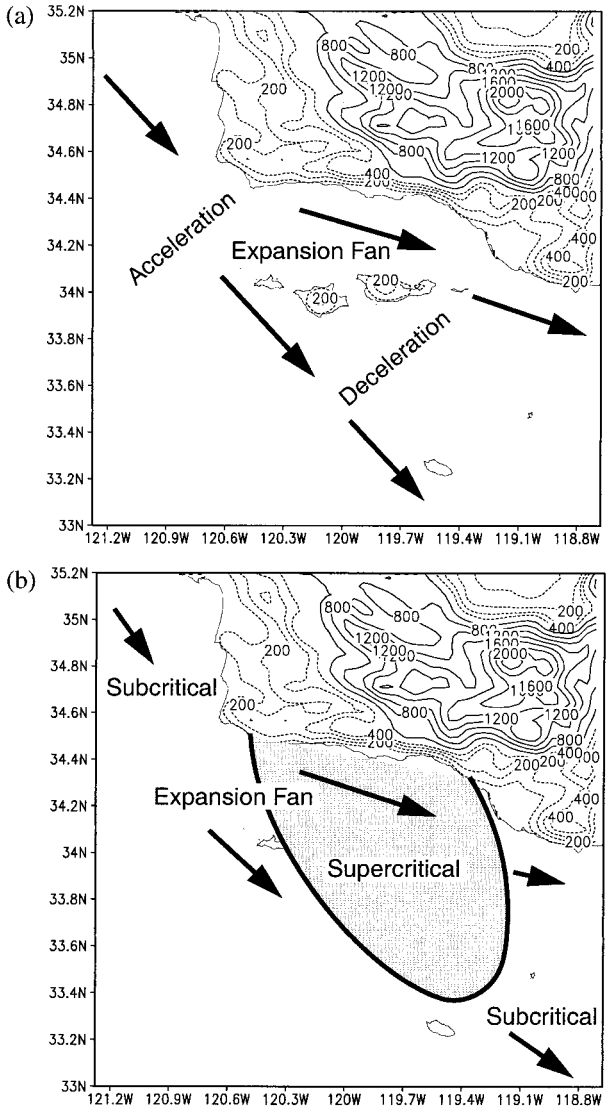

FIG. 3. Schematic showing characteristics of (a) supercritical and (b) transcritical flow over the SBC.

by cooling at night over the Santa Ynez Mountains could propagate westward toward PC and cause a relaxation of the supercritical acceleration over the western SBC.

Summertime flow conditions over the SBC generally show a systematic behavior that depends on the strength and orientation of the synoptic-scale pressure gradient, the MBL depth, and the time of the day. For example, in Fig. 2 we note that the flow increases and diverges when rounding PC, denoting an expansion fan behavior as expected for a supercritical or transcritical hydraulic flow. Also shown is a diurnal cycle in the strength of the flow and a region of weak winds in the lee of PC, indicating a possible separation of the southward prevailing winds from the local circulation over the SBC region similar to the trapped disturbance predictions in Rogerson (1999). Simulation of these flow features cannot be easily performed using shallow water models (e.g., Eddington 1985) because of changes in the layer stratification and horizontal pressure gradients forced by diabatic heating. To accurately simulate stratified, heated flow over the SBC requires a fully three-dimensional mesoscale model including the effects of surface fluxes and vertical stratification. Here, we apply a mesoscale model to examine three commonly observed flow patterns over the SBC that have similar large-scale flow forcing. Our goals in simulating these three cases are to 1) determine if high-resolution mesoscale models can qualitatively predict the marine boundary layer winds over the SBC, 2) assess whether flow pattern over the SBC is consistent with hydraulic flow theory, and 3) determine what factors control the diurnal variability of SBC winds.

To address these goals, we selected cases that had different initial MBL depth and a strong diurnal signal in the surface wind fields. Cases were limited to days with moderate to strong northwest winds at the western end of the SBC, which is the dominant pattern in the summertime SBC climatology (see Fig. 2 and Dorman et al. 2000). Using the mesoscale model, we examine the diurnal evolution of each flow scenario and assess the importance of hydraulic effects through changes in the MBL depth, Froude number, and local momentum balance. Our working hypothesis is that the basic northwest flow pattern over the western SBC can be described as either a supercritical or transcritical hydraulic flow, with heating causing a diurnal modulation of the winds via changes in the cross-shore pressure gradient over the central SBC. For transcritical flows, elevation of the MBL by a propagating disturbance causes a reduction in winds over the SBC, but these effects are ultimately trapped by the supercritical flow region at PC (following Rogerson 1999).

The paper is organized as follows. In section 2, we describe the model along with the initialization procedure. Three case studies are presented in section 3 focusing on the observed upper-air conditions and comparisons between the simulated and measured surface wind fields. Section 4 presents an analysis of the modeled flow characteristics and how they relate to bounded hydraulic flow theory. We also examine the momentum budget over the SBC to determine factors controlling the local flow pattern and formation of horizontal shear in the surface wind fields. Conclusions are presented in section 5.

2. Model description

The model used in this study is the three-dimensional, nonhydrostatic, Advanced Regional Prediction System (ARPS) developed by the Center for the Analysis and Prediction of Storms at the University of Oklahoma (Xue et al. 1995). ARPS is based on a terrain-following coordinate system with surface boundary fluxes prescribed using similarity profiles from Byun (1990) and

variable surface roughness over the ocean (Anderson 1993). The model does not have an explicit boundary layer parameterization (e.g., Troen and Mahrt 1986) but simulates boundary layer development using an intermediate turbulence closure model based on Sun and Chang (1986). The model simulates surface conditions using a radiation parameterization for incoming solar and outgoing longwave radiative flux and surface characterization from Kidwell (1990). Surface temperature of the ocean is set according to input fields from the National Centers for Environmental Prediction Eta Model. A more thorough description of the ARPS model can be obtained from the ARPS Users Manual, available from the University of Oklahoma Web site (http://www.caps.ou.edu/ARPS).

Simulations were performed using a one-way nested grid configuration (ARPS does not have two-way nesting) with three levels of horizontal grid resolution: 36, 12, and 4 km. Grid dimensions of 60 × 60 in the horizontal direction and 32 levels in the vertical were applied for all resolutions, with the 36- and 12-km grids centered at 34°N, 119°W and the 4-km grid centered at 34°15′N, 120°W. A stretched grid was employed in the vertical direction, starting with a bottom grid spacing of 20 m, increasing according to a hyperbolic tangent function to 450 m. This grid stretching scheme gave six levels between the surface and 150-m height and a maximum height of 13 930 m. Initialization data and lateral boundary conditions for the 36-km grid were prescribed using 3-hourly analyzed gridded data from the Eta Model. The horizontal resolution of the Eta dataset is ~40 km, with a vertical resolution of 25 hPa in pressure coordinates. Temperature, moisture, pressure, and momentum data from the Eta Model are interpolated vertically and horizontally to the ARPS 36-km grid at the initial time period and to boundary points on the four sides of the model every three hours. Boundary conditions are determined at each model time step by interpolating between the 3-h segments obtained from the archived Eta data. Inner domain boundaries are relaxed from the outer domain values over a buffer zone of five grid points. This ensures a relatively smooth transition between the differing grid resolutions. A similar procedure was performed for the inner grids, but with a 2-h interpolation period.

3. Case studies

Three cases were selected based on a simple criterion that winds at the western end of the SBC (buoy 54) were generally steady from the northwest, while winds at the eastern end (buoy 53) varied. This flow scenario loosely follows the summer climatology (Figs. 1 and 2), so identifying cases was relatively straightforward. As a second criterion, we wanted to examine the role of the synoptic-scale pressure gradient strength and direction, and the MBL depth. Because of the cost of performing high-resolution simulations, we were limited to seven cases for exploration. Of these seven, three were chosen that best represent the above criteria (Table 1). Each of the selected cases is characterized by an offshore surface high pressure system and northwesterly flow along the coast of California, which is typical of the summer. However, there are significant differences in the location of the anticyclone center at sea level and in the strength of the flow along coastal southern California at 850 hPa. Differences between the cases over the PC area are mostly caused by the depth of the MBL and the strength and orientation of the pressure gradient. Both the case 1 and case 3 pressure fields were somewhat similar in orientation near PC, although case 3 had a slightly weaker gradient. Case 2 had a much weaker gradient, but coastal surface winds (as shown later) were nevertheless fairly strong. Our discussion begins with a detailed overview of each case including the observed and predicted surface flow over a 24-h cycle.

TABLE 1. List of cases.

Case	Date	Conditions
1	2 Jul 1998	Deep MBL
2	5 Aug 1998	Shallow MBL
3	Jul 12 1998	Decreasing MBL depth

a. Case 1: 2 July 1998, deep marine boundary layer, strong pressure gradient

The first case represents conditions that occur when surface high pressure is building off the west coast in response to a 500-hPa ridge over the Pacific and a trough moving onshore over northern California (Fig. 4). The MBL in this case is fairly deep (~400 m) and winds at 850 hPa and at the surface are steady at ~15 m s^{-1} from the northwest along the entire coast of California. At the surface, winds remain strong over the western end of the SBC throughout the day (Fig. 5). Along the northern SBC coast, however, local topography provides a sheltering effect so that winds are light and variable near the surface at Santa Barbara (SBA) but still strong at higher levels above 400 m as shown by profiler winds from near the SBA site (Fig. 6a). At buoy 53 (labeled in Fig. 1), winds exhibit a diurnal cycle with strongest velocities in the late afternoon–early evening when land heating is a maximum. Because the MBL is deep, the headlands at PC do not strongly block the flow, so winds during the afternoon tend to sweep across the SBC with only a small change in direction. At night, the formation of a land breeze affects the winds in the eastern SBC, causing the flow to decrease, but without affecting the winds at the western buoy location (buoy 54).

Simulated 10-m winds and pressure for case 1 (Fig. 5, gray) are in good qualitative agreement with the overall characteristics shown in the observations (Fig. 5, bold). In particular, winds at buoy 54 are consistently from the northwest with a velocity of about 15 m s^{-1}, in close agreement with the model at 10-m height. At the eastern

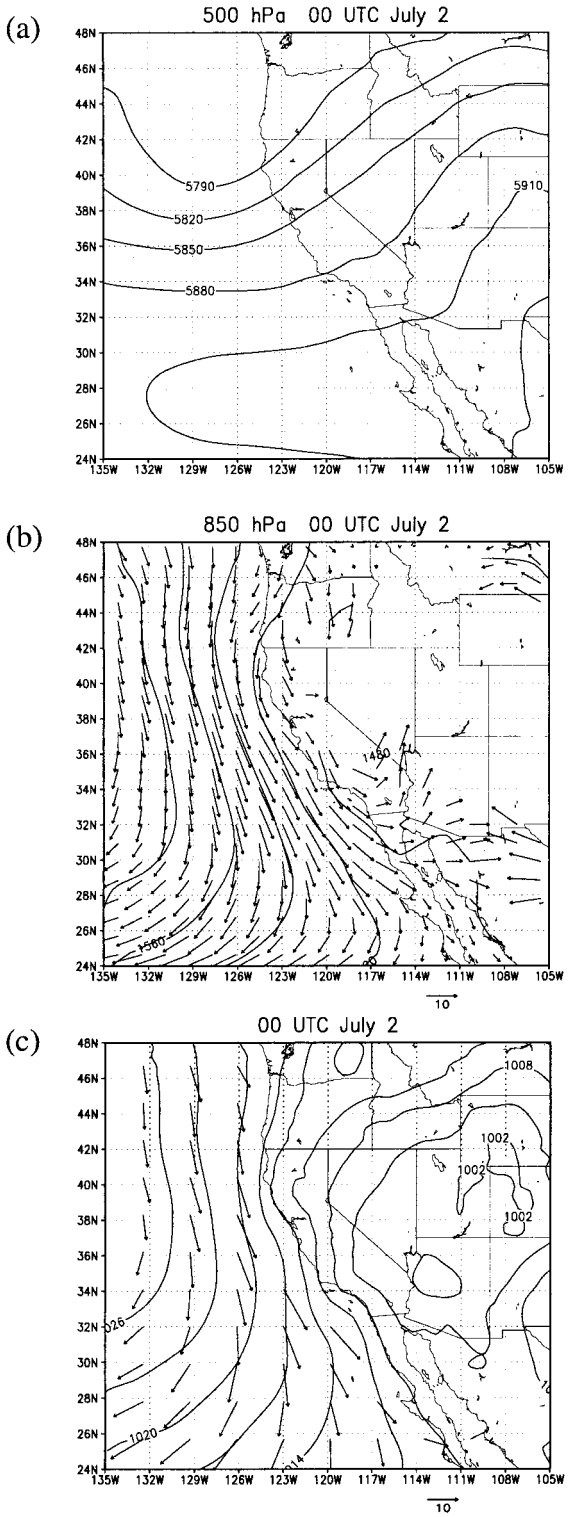

FIG. 4. (a) Geopotential height (m) at 500 hPa, (b) geopotential height (m) with wind vectors (m s^{-1}) at 850 hPa, and (c) sea level pressure (hPa) with wind vectors at 10-m height from 0000 UTC (16 LST) 2 Jul 1998. Gridded data are interpolated from model initialization.

end of the SBC and along the northern shore, winds are stronger in the model in comparison with the observations but show considerable variability and periods of low velocity, particularly near the coastline and east of the channel in the morning. By late afternoon, the winds increase back to the levels of the previous evening, much like the observations, although buoy 25 shows weak winds continuing throughout the period of interest. This is in contrast to the model, which has a distinct diurnal cycle at this location. We note that the station at Vandenburg (labeled VDB in Fig. 1a) is consistently shifted to a more northerly direction in all of the cases, indicating a local bias in direction. Simulated surface pressure has a modest diurnal signal in the eastern SBC as shown by the relaxation in the gradient during the early morning and the strengthening in the gradient in the late afternoon. Overall, comparison of the simulated and observed surface pressure gradient shows good agreement, with pressure at PC ~3–4 hPa greater than the eastern SBC. In all of the simulations, the absolute value of the pressure is different from the observations because of errors in the original Eta Model initialization. However, the absolute pressure value is not significant because the pressure gradient is the dynamically active parameter.

b. Case 2: 5 August 1998, shallow marine boundary layer, weak pressure gradient

Synoptic conditions with our second case are characterized by a 500-hPa ridge centered over the intermountain west (Fig. 7), with a surface heat-induced low pressure, or thermal trough, over the desert southwest, and a surface high pressure off the west coast. The MBL in this case is relatively shallow because of subsidence, and winds aloft are weak as shown by the 850-hPa wind fields in Fig. 7. In response, winds over the SBC are strongly influenced by the topography and diurnal heating, forming a cyclonic circulation during the early morning hours that switches to a westerly flow in the late afternoon and evening (Fig. 8). Profiler winds at SBA also display a pronounced diurnal cycle with winds below ~600 m changing from northwesterly to easterly during nighttime and becoming more westerly in the late afternoon (Fig. 6b).

Simulated surface winds show a behavior similar to the observations, with strong westerly winds at 0600 UTC that relax in the early morning and form a southeasterly flow along the coast (Fig. 8). Heating gradually reestablishes the westerly winds in the afternoon and early evening as the surface pressure gradient increases in the western SBC. Overall, the surface pressure over the SBC oscillates with weak gradients at night that strengthen in response to surface heating and the dynamic effects of the northwest flow around PC. Interestingly, the observed pressure at buoys 54 and 53 do not show a significant gradient along the SBC. This is consistent with the model results that indicate a trough along the northern coast and a relatively weak east–west

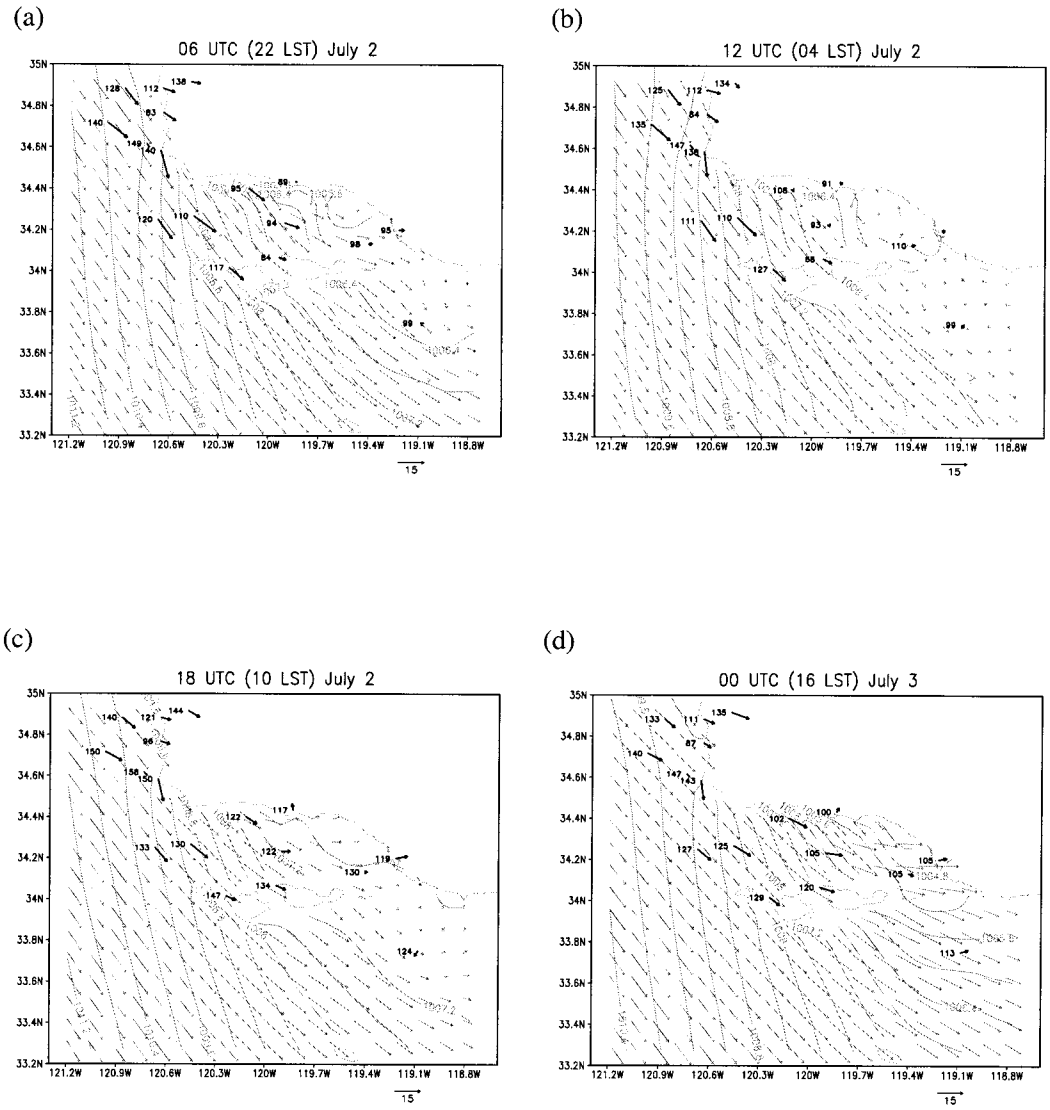

FIG. 5. Surface station vectors and pressure values (bold), along with gridded simulated winds at 10 m (gray) for (a) 0600 UTC, (b) 1200 UTC, and (c) 1800 UTC on 2 Jul 1998 and (d) 0000 UTC on 3 Jul 1998. Gridded winds are plotted every other grid point.

gradient of surface pressure over the southern section of the channel. Most of the wind acceleration from pressure forcing occurs between PC and the central SBC as shown by the difference in pressure between stations on PC and buoy 54. East of buoy 54, the winds gradually decrease in velocity. As in case 1, the model overpredicts the strength of the surface winds east of the Channel Islands, as shown by comparing buoy 25 with the model winds at 00 UTC (16 LST).

c. Case 3: 12 July 1998, offshore flow

The last case represents upper level conditions that are between the strong northwest forcing of case 1 and the locally forced flows of case 2. At 500 hPa, the flow is nearly zonal with weak winds over the study region (Fig. 9). The 850-hPa flow is characterized by a trough over southern California with mostly northerly winds along the coast north and west of the Los Angeles basin. As a result, winds over the SBC are generally offshore aloft and tend to modify the MBL depth during the period of interest. Winds over the SBC with this case are similar to case 2, with strong westerlies in the early evening that relax in the early morning and are replaced by weak southeasterly winds (Fig. 10). Daytime heating reestablishes the onshore pressure gradient, causing westerly winds to return over the SBC in the late afternoon. Profiler winds reflect the diurnal pattern, beginning the day with northwest winds aloft that switch rapidly at sunset to a more easterly direction (Fig. 6c). As heating progresses during the afternoon, the winds gradually back to the west-northwest and accelerate.

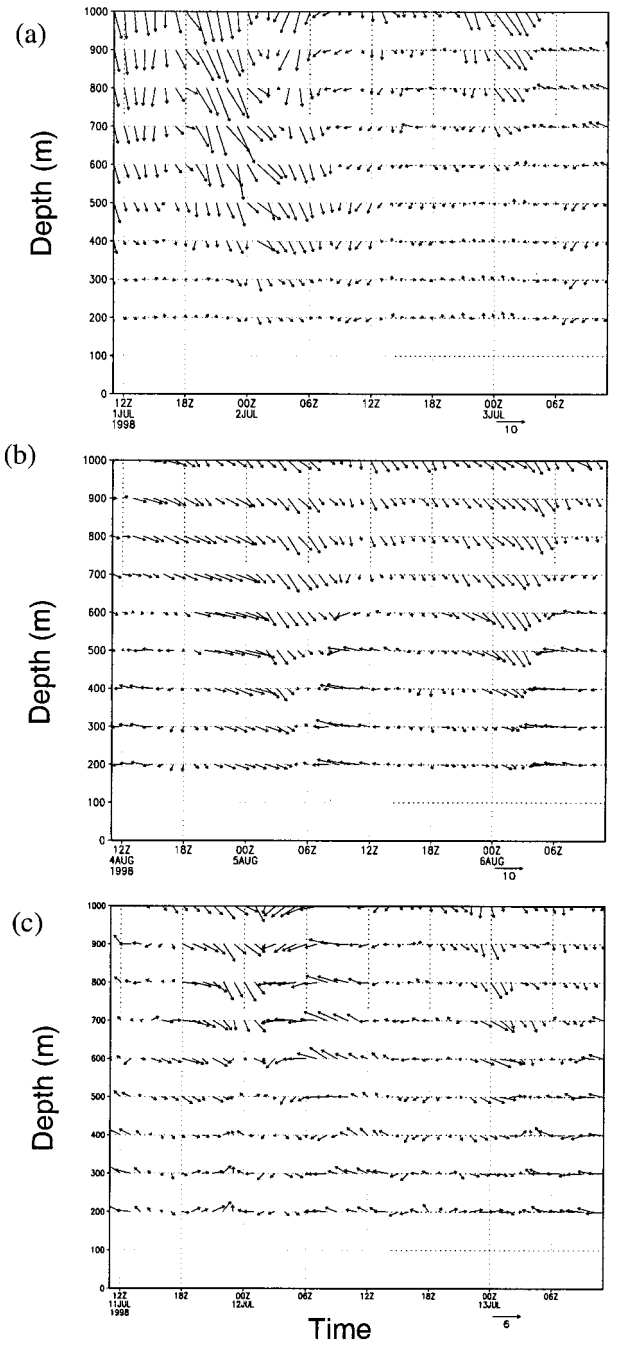

FIG. 6. Time-depth plot of horizontal wind vectors (m s^{-1}) measured with a radar profiler located at the Santa Barbara airport in Goleta, CA, on (a) 2 Jul, (b) 5 Aug, (c) 12 Jul 1998. The location of the profiler is indicated in Fig. 1.

Plots of the 10-m winds and pressure for case 3 are similar to the corresponding fields from case 2. Initially, the pressure field forces a typical northwest flow scenario with the wind direction generally following the coastline as it passes PC. Overnight, the winds decrease rapidly over the SBC and turn to a southeasterly direction over the eastern end of the channel. At the same

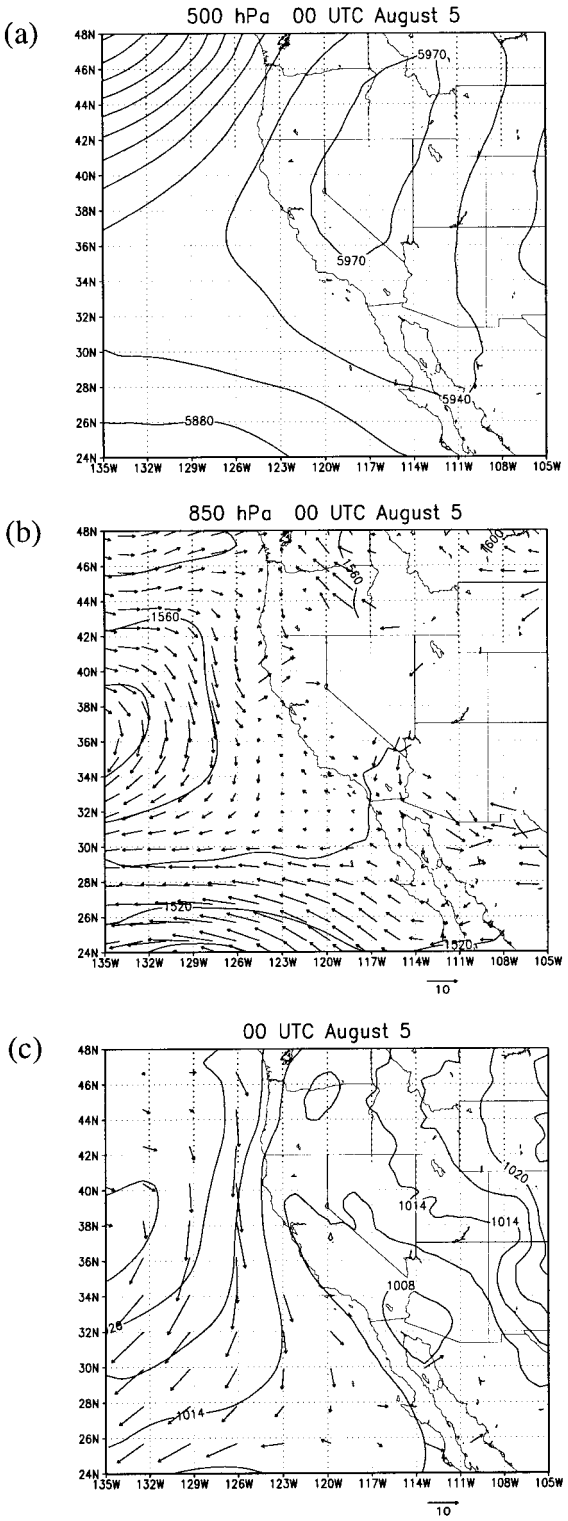

FIG. 7. As in Fig. 4, but for 5 Aug 1998.

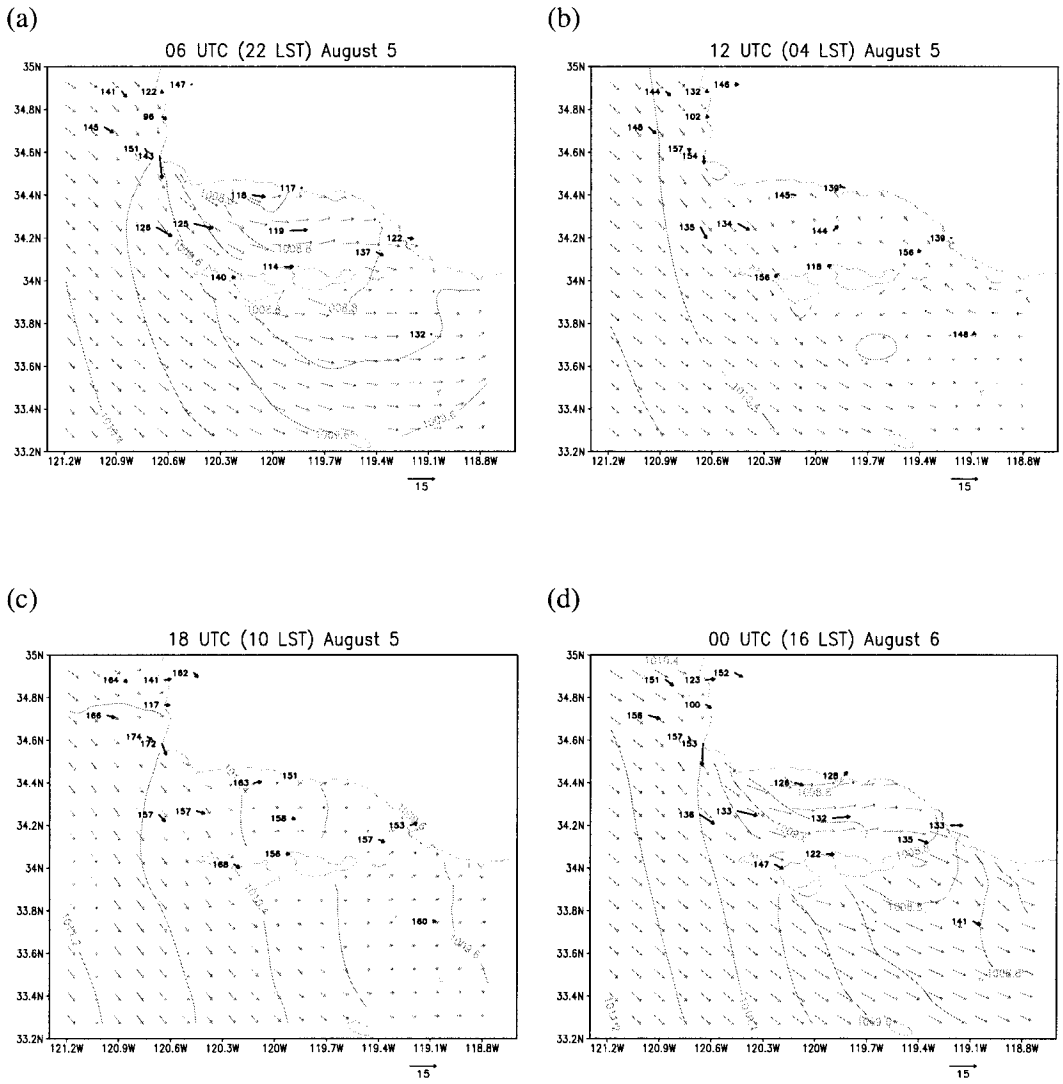

FIG. 8. As in Fig. 5 but on 5–6 Aug 1998.

time, a weak low pressure appears south of the Channel Islands with a trough over the western SBC. Daytime heating disrupts this pattern, so that by 1800 UTC winds are already weak westerly over much of the region. By 0000 UTC on 13 July, the onshore flow pattern is completely reestablished, although the pressure gradient is weaker than in the morning because of changes in the synoptic-scale forcing. Because of the weaker gradient, the Channel Islands have a stronger influence on the flow as indicated by the cyclonic flow curvature and lower pressure in the lee of the islands. Simulated winds are in reasonable agreement with the observations; however, the surface pressure gradient is less consistent with the 0000 UTC observations indicating that the model has located the SBC trough too far east. Also, the observations maintain a steady large-scale pressure gradient, whereas the simulated domain-scale pressure gradient has decreased by 0000 UTC on 13 July.

4. Analysis

a. Marine boundary layer depth and Froude number

We begin our analysis by examining the behavior of the MBL depth for each of the simulations. Simplified slab models of coastal flow based on hydraulic theory (e.g., Samelson 1992; Rogerson 1999) point out the importance of the MBL depth along with the large-scale pressure gradient force or background flow rate. As the MBL interacts with the coastal terrain, mass balance is maintained by changes in the MBL depth and the local velocity. This is demonstrated in Fig. 11 showing the MBL depth and wind vectors at 0600 and 0000 UTC for each of the simulations. The depth of the MBL in these plots is calculated by scanning vertically at each grid point over the water until the potential temperature has increased by 10°C in cases 1 and 2 and by 5°C in case 3. Our estimate of the MBL depth is not exact

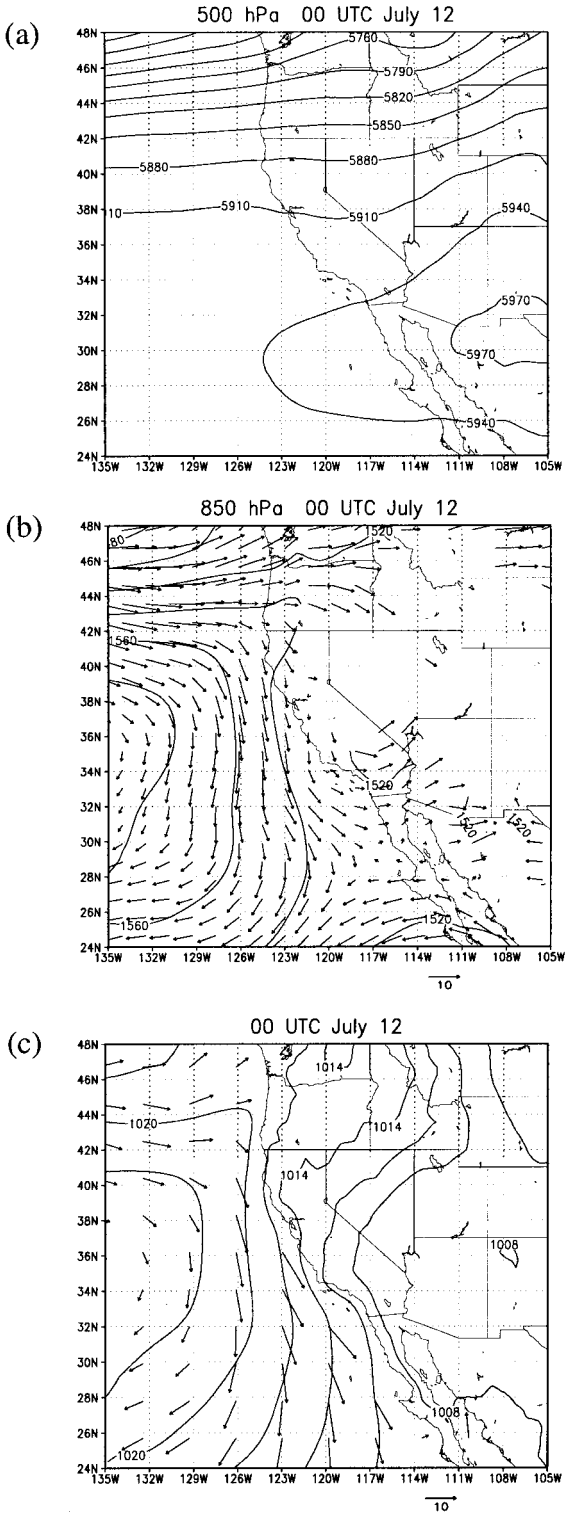

FIG. 9. As in Fig. 4, but for 12 Jul 1998.

because it includes a portion of the capping inversion, but nonetheless it provides an adequate qualitative measure.

For case 1, the MBL has an upstream depth of ~300–400 m, so that the boundary layer flow is affected mostly by the higher terrain that is east of Point Conception. As a consequence, air passing over PC is not diverted by the local terrain and continues southeastward with little change in direction (although surface roughness and heat flux do affect the boundary layer structure). Farther east, however, the much higher terrain associated with the Santa Ynez Mountains creates an effective block of the MBL, sheltering the north and eastern coastlines of the SBC during the nighttime when the surface boundary layer is stable. During the afternoon hours (0000 UTC), interior heating augments the existing surface pressure gradient and destroys the nighttime stable layer. At this time the MBL interacts with the Santa Ynez Mountains much like a fast-moving supercritical flow. Downstream from the Santa Ynez Mountains (over the eastern SBC), the flow exhibits a variable MBL depth and a weak expansion fan in the lee of the topographic feature.

In contrast to case 1, cases 2 and 3 are characterized by a shallower MBL with depths of ~200 m over the open ocean and as low as 40 m over the SBC. An exception to this is case 3 later in the simulation period (0000 UTC 13 July), when the MBL depth is ~100 m over the open ocean. As shown later in this section, the flow aloft in case 3 is offshore causing the MBL depth to decrease throughout the study period. When the MBL is shallow, coastal terrain has a more significant affect on the flow. For example, in case 2 and 3, the MBL depth decreases in the lee of PC, producing an expansion fan and acceleration extending from the western SBC across the channel, again suggesting supercritical or transcritical hydraulically controlled flow (e.g., Fig. 3). A weaker MBL decrease and acceleration is noted in the lee of the Channel Islands, indicating that the combined topography of the islands acts as a semicontinuous obstruction to the flow. This effect is particularly noticeable in case 3, where the surface winds turn sharply behind the channel islands at 0000 UTC on 13 July.

A number of studies have applied hydraulic theory to flow along a varying coastline (e.g., Winant et al. 1988; Samelson 1992; Burk et al. 1999; Rogerson 1999). One of the more realistic modeling studies is presented in Burk et al. (1999; hereafter BHS). By applying a three-dimensional, nonhydrostatic model with an idealized atmosphere and coastline, BHS examined the effects of sub- and supercritical conditions on coastal flows. Their study differed from the present analysis by assuming a vertical wall for representing coastal terrain, no heating, and a strong inversion capping the prescribed MBL. For supercritical flows, they found that the most significant effects of the coastal point appeared in the lee of the obstacle and were characterized by a decrease in the surface pressure and an increase in the

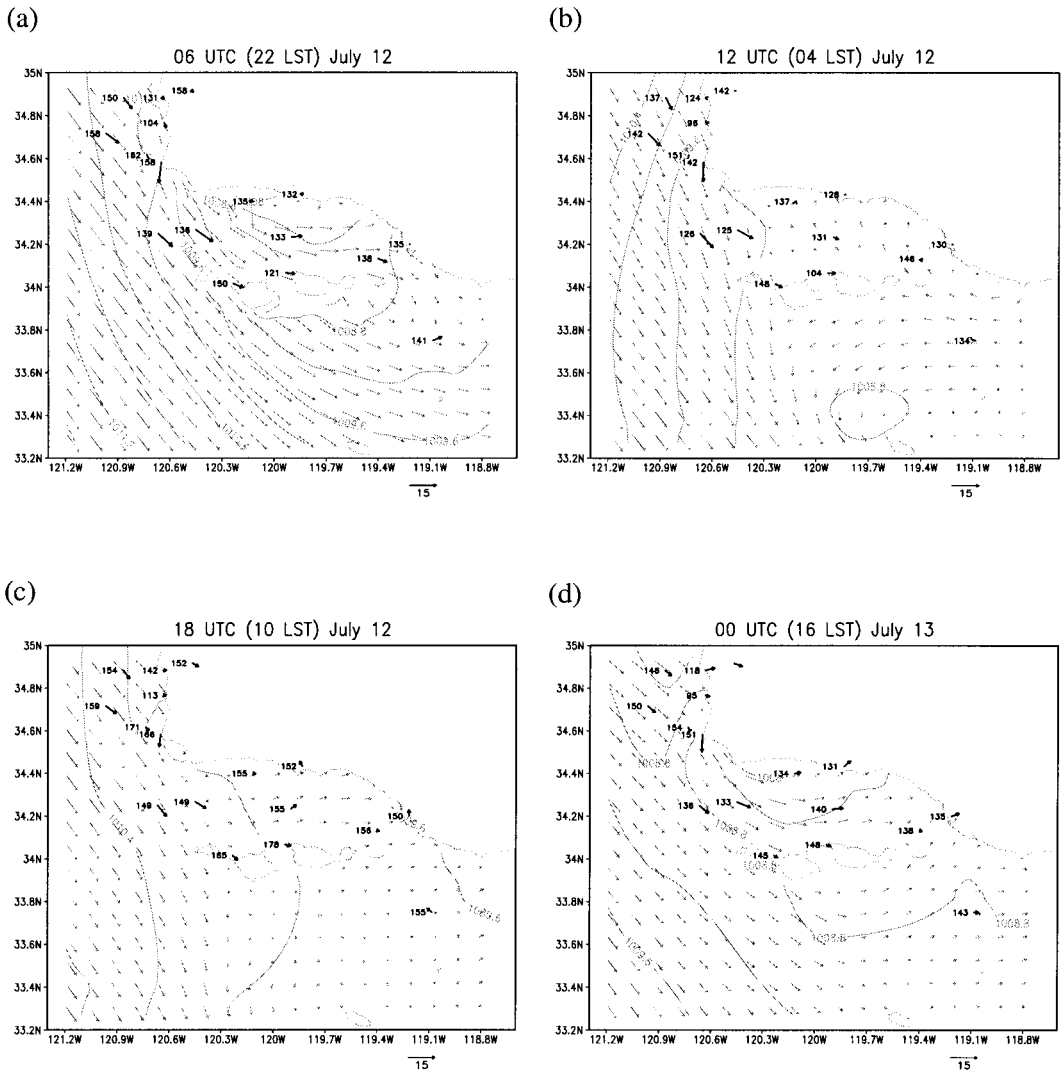

FIG. 10. As in Fig. 5, except for 12–13 Jul 1998.

local Froude number. The strongest acceleration occurred when the flow was transcritical (changed from subcritical to supercritical) when passing the coastal point. They also found that transcritical flow displayed significant vertical structure, a feature previous shallow water model studies could not examine because of the single-layer physics of the models. Using a less sophisticated shallow water model, Rogerson (1999) focused on the behavior of transcritical flows and the effects of perturbations on the region of subcritical flow in the lee of coastal points. These perturbations were able to propagate northward in Rogerson's simulations and caused the formation of a cyclonic circulation as the disturbance became trapped by the supercritical flow around the point.

Many flow features identified in these idealized model studies are evident in the simulations presented here. For example, the strong acceleration of the flow and decrease in MBL depth over the SBC shown in Figs. 11b and 11e is qualitatively similar to transcritical flows presented in BHS and Rogerson (1999). Because of these similarities, we next examine estimates of the Froude number, which, as discussed in the introduction, provides a means of identifying supercritical and transcritical flows. The simulation Froude number is calculated using

$$\mathrm{Fr}_s = \frac{U}{\sqrt{g'h}}, \tag{1}$$

where $g' = g\Delta\theta/\theta$ and $\Delta\theta$ is the change in potential temperature at the top of the MBL. For cases 1 and 2, we took $\Delta\theta = 20$°C, which are values representative of the near-shore stratified flow. For case 3, $\Delta\theta = 10$°C was used because the boundary layer capping inversion was not as strong as in the other cases. In all cases $\theta = 300$ K was used. Because the simulated boundary layer is capped with a variable depth stratified layer and

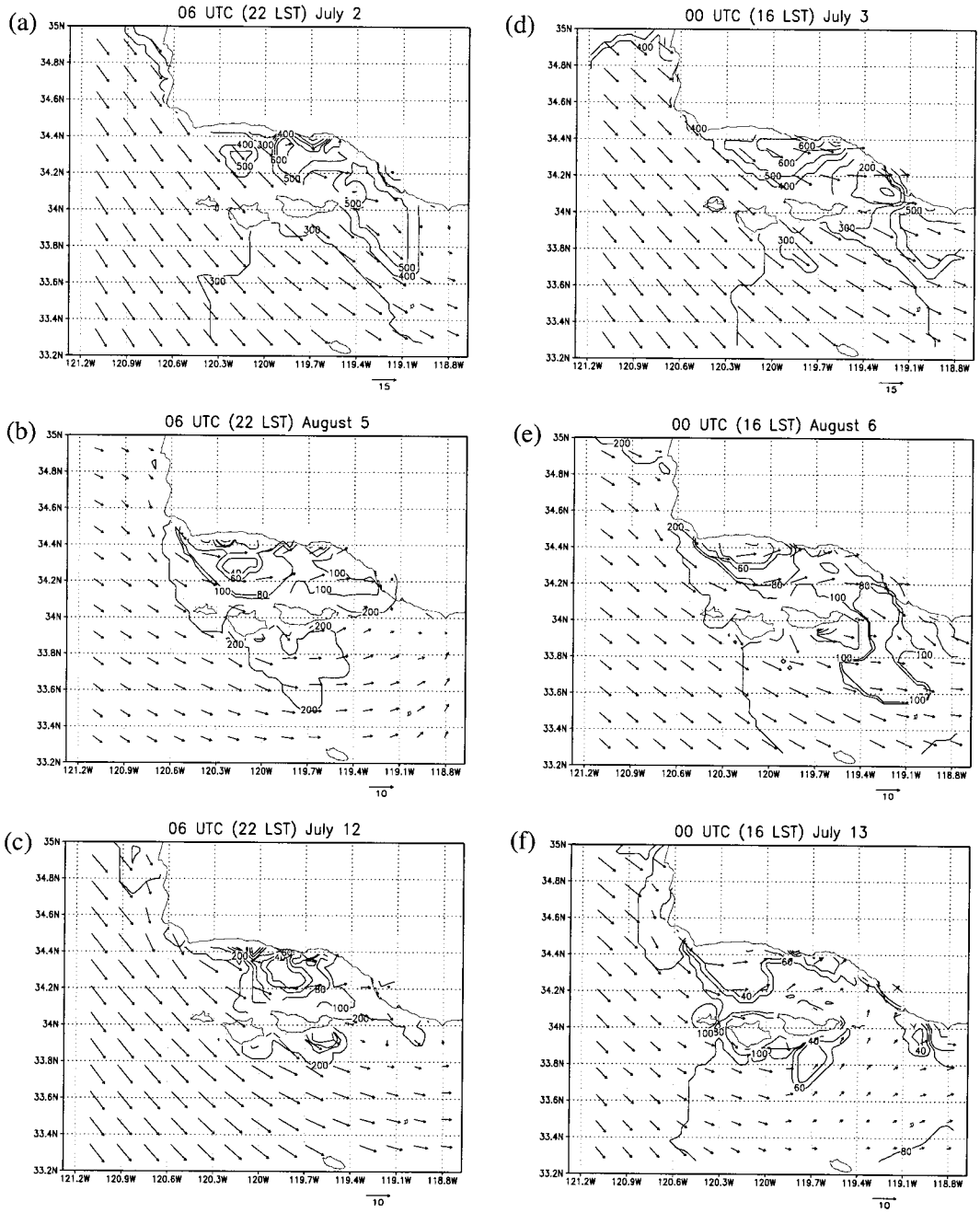

FIG. 11. Simulated marine boundary layer depth (m) and surface wind vectors (every fourth grid point) (m s^{-1}) at 0600 UTC on (a) 2 Jul, (b) 5 Aug, (c) 12 Jul, and at 0000 UTC on (d) 3 Jul, (e) 6 Aug, and (f) 13 Jul 1998. Note that vector scaling is different for 2–3 Jul. Contour levels are every 20 m up to 100 m and then every 100 m.

does not have a clearly defined mixed layer depth, our calculation of Fr_s is not exactly the same as in slab models (e.g., Samelson 1992; Rogerson 1999) or in the idealized simulations of BHS. Also, as pointed out in BHS, Fr_s may not be appropriate for establishing flow criticality because the flow vertical shear can have a strong trapping effect much like stratification and therefore influence the effective h. However, vertical profiles upstream from PC (not shown) indicate that strong vertical shear and stratification are collocated at the top of the MBL, so our estimate of h based on θ is reasonable. We note that because the flow is stratified, our estimate of g' is not representative of the entire domain in every case. However, we found that varying g' for a range of $\Delta\theta$ between 5° and 15°C did not change Fr_s by a significant amount.

Plots of Fr_s (Fig. 12) indicate that for case 1 the flow is supercritical through most of the model domain and

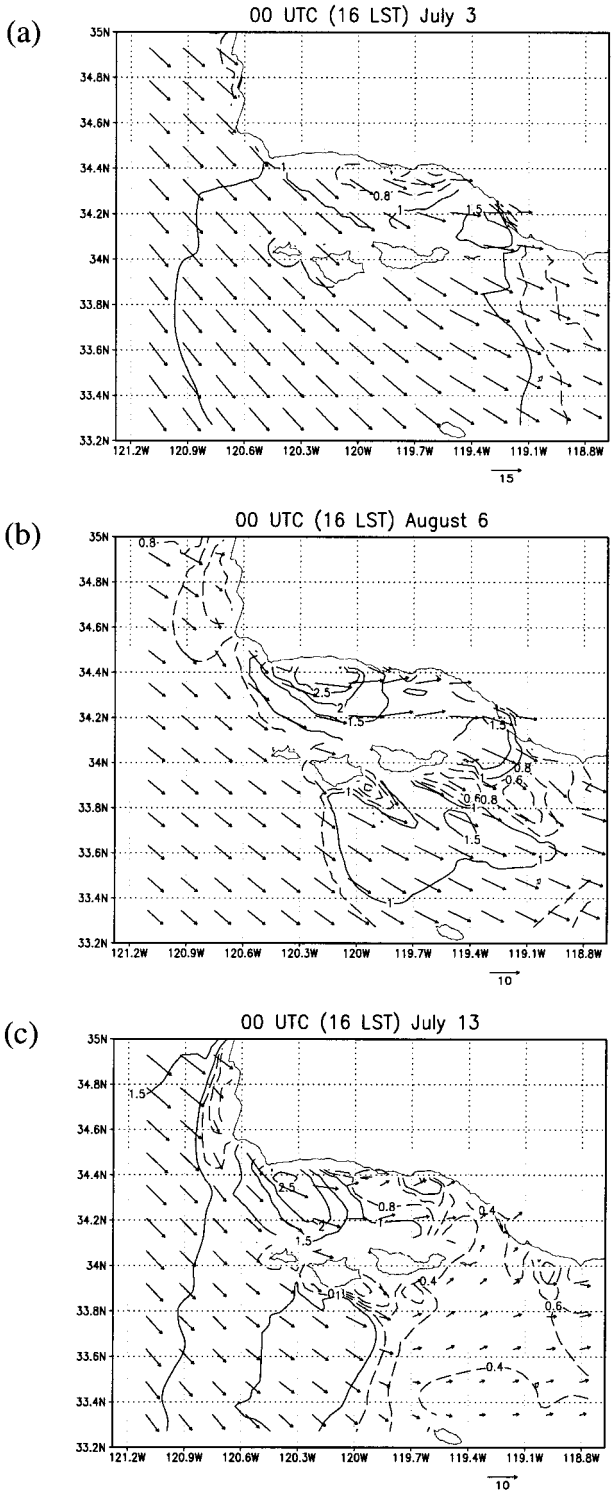

FIG. 12. Froude number and surface wind vector (every fourth grid point) (m s^{-1}) from 0000 UTC on (a) 3 Jul, (b) 6 Aug, and (c) 13 Jul 1998. Contours below 1.0 are dashed. Note that vector scaling is different for 3 Jul. Contour interval is 0.2 for Froude number below 1.0 and 0.5 for Froude number above 1.0.

does not exhibit a strong shift from sub- to supercritical flow except for very near the northern coastline of SBC. Here, the subcritical flow is likely a result of local blocking by the Santa Ynez Mountains as discussed above. Comparing our simulations with the benchmark case in BHS, we find similar features for supercritical flow: increased Fr_s over a broad region south of PC (and the Channel Islands) along with turning of the wind direction and lower pressure (all characteristics of a supercritical flow expansion fan). An interesting observation is that the upstream flow in our simulations does not follow the coastline as much as in BHS. This is because the coastline ~75 km north of PC turns to a more northwesterly direction, setting up a concave coastline (e.g., see map in Fig. 4). Consequently, the orientation of PC relative to the flow is much less than the ~90° indicated by the coastline map. In fact, the orientation is closer to the 30° used in BHS, which helps explain the similarity between the idealized cases and the simulations presented here.

In case 2, Fr_s is more typical of a transcritical flow condition (Fig. 12b). Upstream from PC, $Fr_s < 1$, denoting subcritical conditions. Upon rounding PC, the MBL depth lowers rapidly and the flow velocity increases so that the flow becomes supercritical over most of the SBC and south of the Channel Islands. Subcritical conditions return at the eastern end of the channel where the flow speed decreases and the MBL depth rises. Case 3 shows similar flow features (Fig. 12c), although the upstream Fr_s is greater than 1, indicating that the flow should be supercritical rather than transcritical. The inconsistent behavior of case 3 is probably a result of the transition that is occurring in the large-scale forcing noted earlier. We found that the MBL depth decreased significantly over the period of the simulation causing the flow to transition from a strong, relatively uniform flow representative of a deep MBL, to a flow more affected by the near-shore coastal terrain, in line with the shallow MBL case 2 example. Two mechanisms that can decrease the depth of the MBL are subsidence and/or horizontal advection. In this case, we believe the MBL depth decreased in response to offshore advection of relatively warm air created over the inland regions of California. Meridional vertical cross sections of the potential temperature and meridional velocity component at 121°W (Fig. 13) show how warm air aloft is advected southward from north of PC. The air is heated during the previous day above the desert interior and then forced over the Coastal Range by the offshore winds, displacing the cooler marine air mass. The flow is not strong enough to completely destroy the MBL, but it overrides the near-surface layer, creating a ~100-m-deep MBL. Examination of the potential temperature and velocity fields at 100-m height from the 12-km resolution simulation demonstrates the offshore extent of this air mass by the middle of the night (Fig. 14).

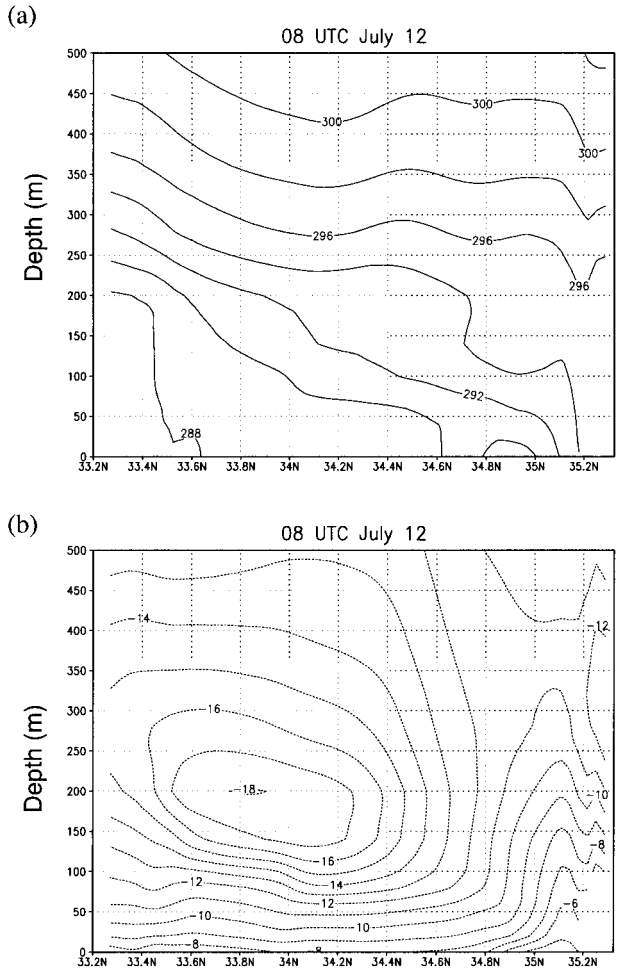

FIG. 13. Meridional–vertical cross sections at 121°W of the simulated (a) potential temperature (K) and (b) meridional velocity, v, (m s^{-1}) at 0800 UTC on 12 Jul 1998.

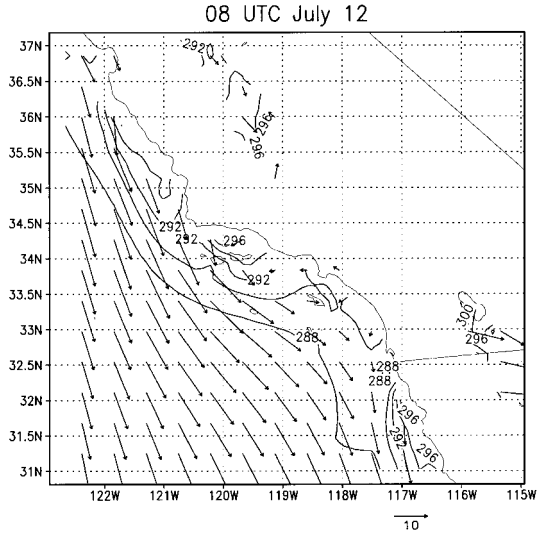

FIG. 14. Simulated potential temperature (K) and horizontal wind vectors (m s^{-1}) at 100-m height from 0800 UTC on 12 Jul 1998. These data are taken from the 12-km resolution simulation.

b. Diurnal effects and the momentum budget

As pointed out in section 3, diurnal heating in all of the cases has a significant effect on the boundary layer circulation generated by the interaction of the flow with PC. In particular, case 2 undergoes a strong daily cycle highlighted by the formation of a cyclonic eddy over the central SBC in the early morning hours (Fig. 8). Plots of Fr_s for this case (Fig. 15) corresponding to the four time periods shown in Fig. 8 indicate that the flow undergoes a transition from transcritical in the afternoon and early evening to subcritical during the nighttime and early morning time periods before returning to transcritical state during the daytime hours. Examination of the upstream value of Fr_s (not shown) does not show a similar cycle, indicating that large-scale changes are probably not responsible for the flow transition.

The flow behavior in case 2 closely resembles trapped disturbance simulations performed by Rogerson (1999) using a shallow water model for transcritical flows with an idealized coastline (resembling the schematic in Fig. 3). Rogerson imposed upward MBL perturbations in the subcritical flow region downstream from a coastal point to see if the northward propagation of coastal trapped waves could be halted by changes in the coastline orientation. The domain size considered in this study was similar in scale to the current problem (~200 km) with a coastal angle of 35°, MBL depth of ~300 m, and wind speeds of ~10 m s^{-1} (multiple coastal points were examined; however, the separation between the points was comparatively small). Rogerson demonstrated that for transcritical flows, perturbations initialized south of coastal points can greatly reduce the area of supercritical flow in the lee of the coastal obstruction. For strong perturbations, a cyclonic circulation forms as the disturbance propagates northward in the subcritical flow region, with the flow ultimately changing from transcritical to a completely subcritical flow, indicating that the coastline change has not completely trapped the wave disturbance. The timescale for propagation in these simulations was dependent on the strength of the perturbation, but it generally ranged from ~8 to ~14 hours, with stronger perturbations propagating at a faster rate.

In order for the trapping mechanism identified by Rogerson to apply in the SBC case, a mechanism is needed to elevate the MBL at the eastern end of the SBC. For case 2, the relaxation of the afternoon sea breeze and the formation of a nighttime land breeze is a likely candidate for lifting the MBL. As the land surface cools at night, the inland pressure increases, eventually leading to an offshore velocity component, or ''land breeze'' and advection of cooler air over the SBC from the land surface. Vertical cross section plots of the potential temperature taken from 34.2°N (Fig. 16) demonstrate the evolution of the land breeze in the simu-

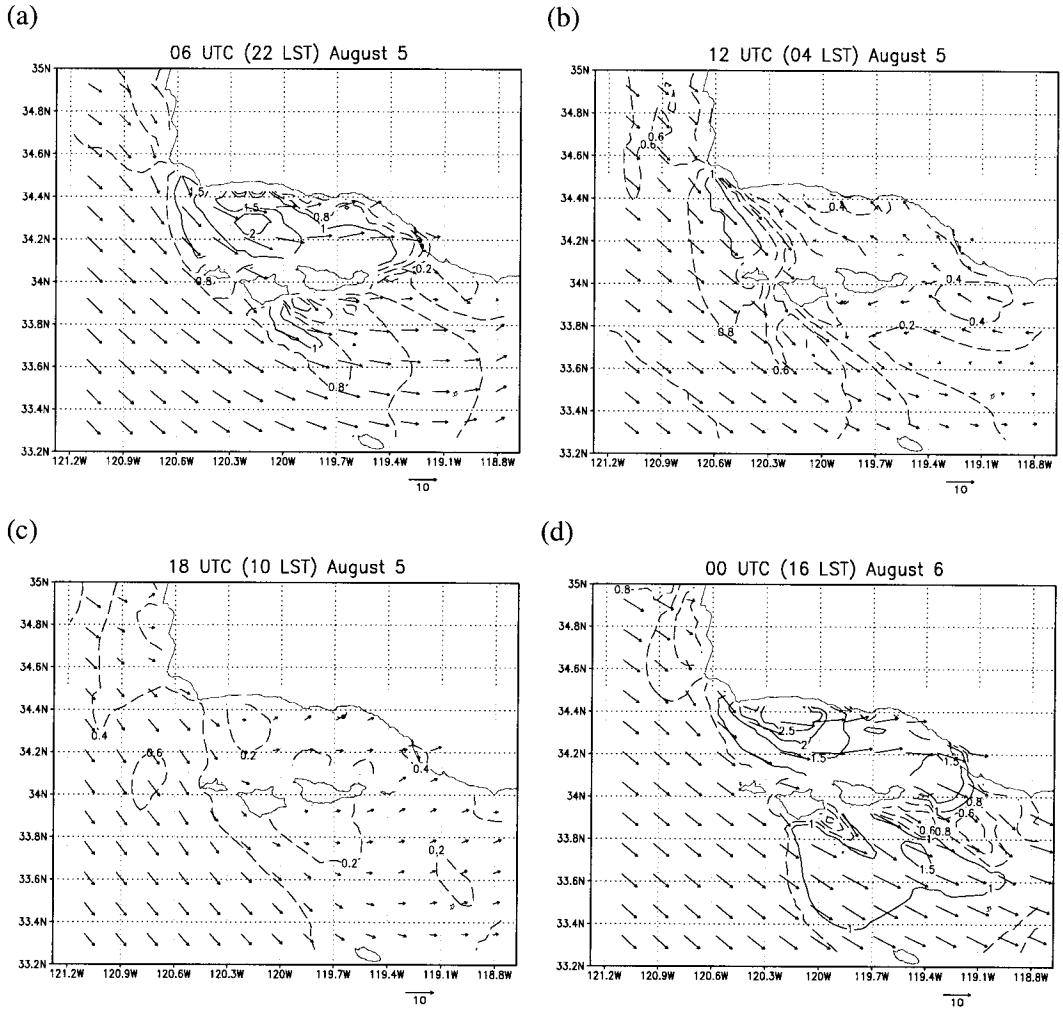

FIG. 15. Froude number and surface wind vectors (every fourth grid point) (m s^{-1}) from (a) 0600 UTC (2200 LST), (b) 1200 UTC (0400 LST), (c) 1800 UTC (1000 LST), and (d) 0000 UTC (1600 LST) on 5 and 6 Aug 1998. Froude numbers below 1 are dashed. Contours for Froude number are every 0.2 for values below 1, and 0.5 for values above 1.

lation between 0800 and 1200 UTC. During this time period, cooling along the mountains on the northern and eastern edge of the SBC forms a pool of cooler air that gradually propagates westward over the channel as an internal gravity wave or bore. The leading edge of this pool (indicated by the vertical gray bar in Fig. 16) is located near 119.4°W at 0800 UTC and near 120°W at 1200 UTC, indicating a propagation speed of ~7–8 m s^{-1}, which is close to the MBL gravity wave velocity defined by $C_g = \sqrt{g'h} = 8.1$ m s^{-1}, using the same values for g' and h used in the Fr_s calculation. In case 2, the land breeze perturbation is strong enough to eliminate the supercritical flow region at the western end of the SBC by 1800 UTC (1000 LST). However, we do not see a propagating disturbance north of PC, which is consistent with Rogerson's results showing strong attenuation of the coastal disturbance while passing through the supercritical flow region.

Examination of the horizontal momentum budget provides a means of connecting variations in the pressure with changes in the velocity fields. Horizontal momentum is governed by

$$\frac{\partial u}{\partial t} = -\mathbf{V}\cdot\nabla u - \frac{1}{\rho}\frac{\partial P}{\partial x} + fv + F_x$$

$$\frac{\partial v}{\partial t} = -\mathbf{V}\cdot\nabla v - \frac{1}{\rho}\frac{\partial P}{\partial y} - fu + F_y, \qquad (2)$$

I II III IV

where $\mathbf{V}$ is the total velocity vector composed of the zonal and meridional velocity components, u and v, respectively, and the vertical velocity; P is the pressure; f is the Coriolis term; and F_x and F_y represent subgrid mixing terms. Budget terms on the right-hand side of (2) represent, respectively, I) nonlinear advection, II) pressure gradient forcing, III) Coriolis effect, and IV) subgrid-scale mixing.

We focus our analysis of the momentum budget on

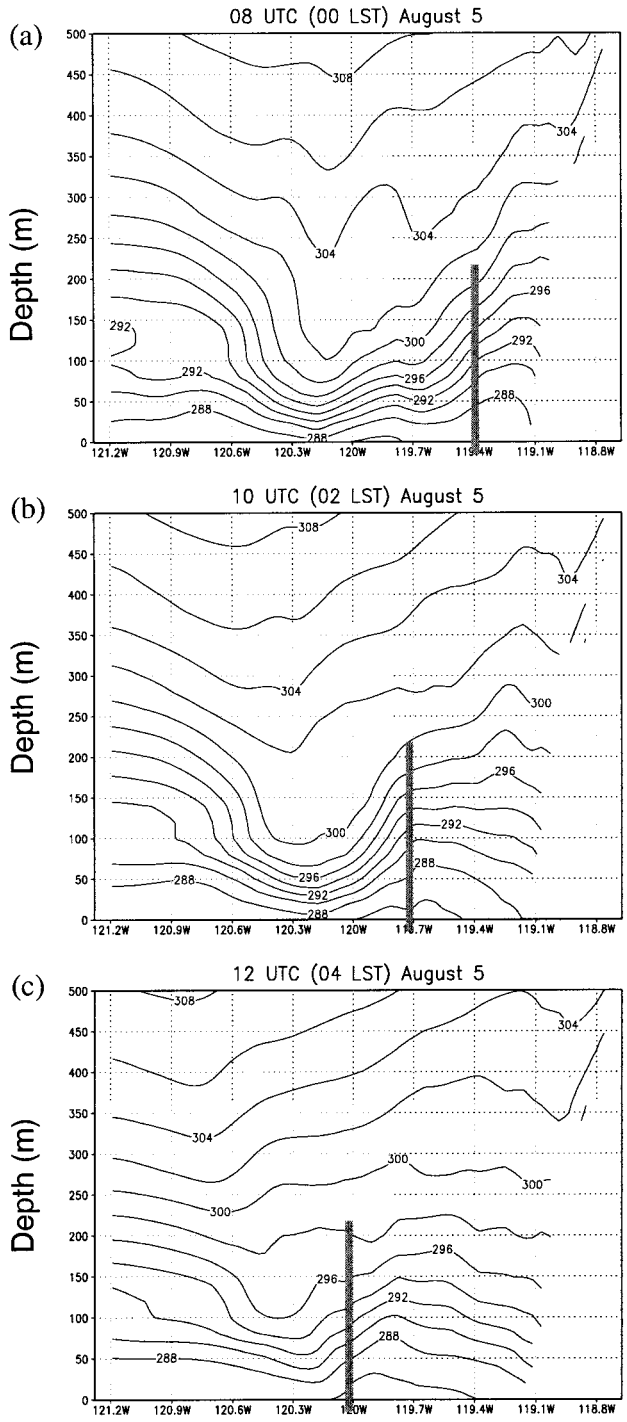

FIG. 16. Zonal–vertical cross sections at 34.2°N of potential temperature (K) at (a) 0800 UTC (0000 LST), (b) 1000 UTC (0200 LST), and (c) 1200 UTC (0400 LST). Also shown is the position of the land breeze–induced disturbance (gray bar), which propagates from east to west at ~7–8 m s^{-1}.

Case 2 by presenting Hovmöller plots of the zonal and meridional momentum budget terms at 20-m height (Figs. 17 and 18, respectively) as a function of time and longitude at 34.2°N. Initially, the u and v pressure terms are both positive, indicating an onshore acceleration east of PC. For the v component west of ~119.6°W, much of this acceleration is offset by the v advection term representing the transport of southerly moving air from the open ocean. In contrast, over the eastern SBC the v advection term compounds the pressure term, forcing a significant northerly flow (as shown at 1200 UTC in Fig. 8b). As the interior cools, the u pressure term reverses direction causing a reduction in zonal velocity that propagates westward to about 120°W at 1200 UTC, roughly following the progression of the potential temperature perturbation discussed above. Reduction in u during the night, as shown in Figs. 8b and 8c, is partially offset by the advection term, which indicates transport of eastward momentum from the open ocean west of PC. Frictional effects combine with the pressure term, causing the zonal wind to decrease even more. After 1800 UTC, the u and v pressure terms east of PC become positive as interior heating reestablishes the afternoon sea breeze. This is particularly true just south of PC at ~120.3°W where the flow shows a strong eastward acceleration from the combined pressure and advection terms. The v component pressure term also increases rapidly in this region but is strongly offset by a decrease in the advection term as southward momentum is advected from the open ocean west of PC. The onshore pressure gradient created by inland heating reestablishes conditions favorable for transcritical flow by decreasing the depth of the MBL over the central and eastern sections of the SBC.

Coriolis forcing is generally of secondary importance relative to the other budget terms in the momentum budget for the SBC circulation, particularly east of ~120°W, indicating the strong ageostrophic forcing produced by the interaction of the stable MBL with the coastal terrain. This is consistent with the hypothesis that the flow is supercritical over the SBC region, although other aspects of the momentum budget, such as the strong mixing term and changes in the pressure caused by diurnal heating, alter the flow field from a purely hydraulic response. BHS point out that subcritical flow approaches geostrophic balance in the cross-coast direction. In contrast, we find that the Coriolis term is of the same order as pressure, advection, and mixing over the subcritical regions (i.e., open ocean).

Qualitative comparisons of the simulated momentum budget terms with observed budget estimates reported in Samelson and Lentz (1994; hereafter SL) show similar behavior for the model fields. In SL, measurements taken from buoys off of northern California were used to estimate the momentum balance for the alongshore and cross-shore velocity components. Because the SBC coastline is oriented nearly east–west, we consider the u component as alongshore and the v component as

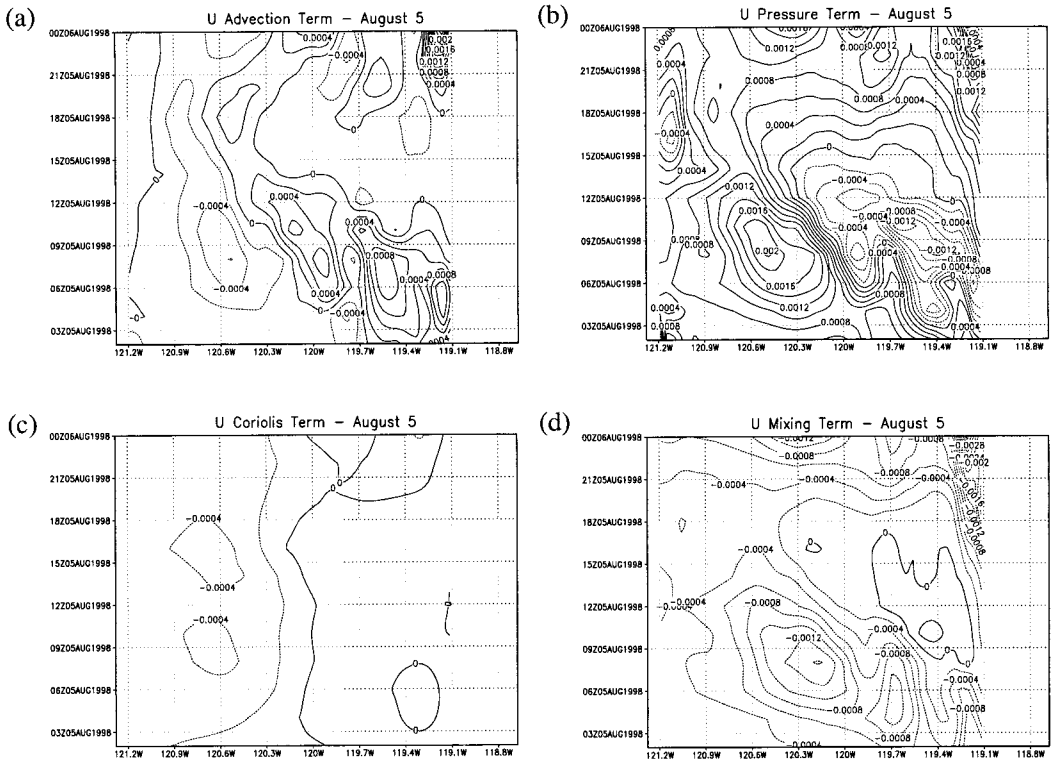

FIG. 17. Longitude–time Hovmöller plots from 34.2°N on 5 Aug 1998 (case 1) at 20 m above sea level of (a) advection term (I), (b) pressure gradient term (II), (c) Coriolis term (III), and (d) subgrid-scale mixing term (IV) from the zonal momentum equation. Contours are every 0.0002 m s^{-2}.

cross-shore. In their analysis, SL determined that the cross-shore momentum budget was dominated by a balance between the ageostrophic acceleration and the cross-shore pressure gradient. A similar balance is noted in Fig. 18 east of PC during the late afternoon and early evening between 0300 and 0900 UTC, when the pressure term is noticeably larger than the other v momentum budget terms. For the alongshore component, SL found that the dominant balance was between the pressure gradient and the vertical mixing terms (or vertical divergence of the stress). Similarly, the simulation results show that the pressure and mixing terms tend to cancel one another during the afternoon and early evening over the SBC. Overall, SL argue that the dominance of ageostrophic acceleration indirectly supports the assumption of supercritical flow in agreement with our Froude number analysis.

5. Conclusions

A nonhydrostatic three-dimensional mesoscale model (ARPS) is used to examine summertime flow characteristics over the SBC region. Typical summertime conditions are represented by a northwesterly flow over the open ocean that is deflected when passing Point Conception, sometimes creating sharp transitions from strong northwest winds to relatively light conditions over horizontal distances of ~10 km. Three cases are presented, each having similar synoptic-scale surface patterns, but with differences in pressure gradient strength and MBL depth. In the first case, the MBL is relatively deep at ~400 m with the strongest relative pressure gradient. Case 2 is characterized by a shallow MBL (~200 m) and a weaker pressure gradient. The last case represents a transition state, with a moderately strong pressure gradient and a decreasing MBL depth from ~200 to ~100 m during the simulation period. All simulations encompass a single day so that diurnal heating effects can be examined.

Comparison of the simulated wind fields with measurements show that the model reproduces many observed flow features. Most importantly, the simulated winds undergo a strong diurnal cycle in agreement with observations, with winds in the eastern SBC alternating from moderate onshore winds in the afternoon to weak, variable winds in the early morning. Persistent differences between the model and observations are mostly confined to the western coastal region of the SBC between Santa Barbara and PC. Offshore winds in this area are at times predicted by the model but are rarely observed in the station data. The model also tends to overpredict winds at the eastern boundary of the model toward the end of the 24-h prediction period, possibly indicating problems in the nested grid configuration.

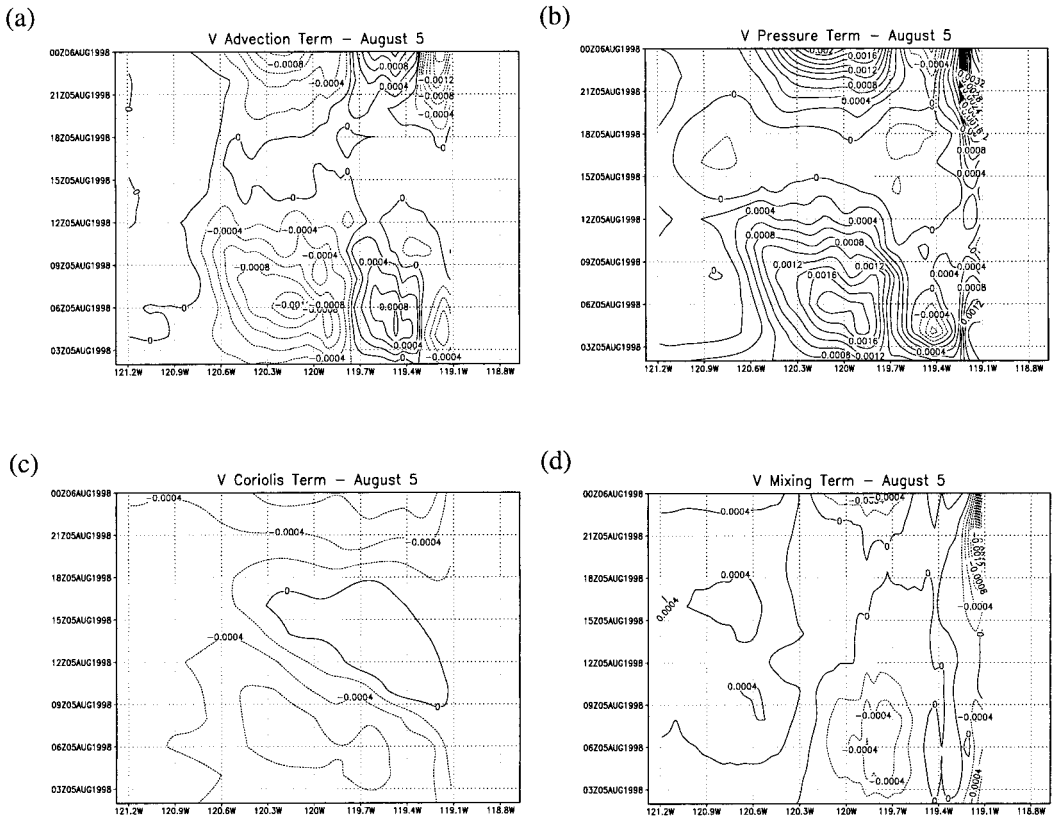

FIG. 18. Same as Fig. 17, but for the meridional velocity component.

Our results show that two main factors control the strength and variability of northwest winds over the SBC region: the strength of the large-scale pressure gradient (and upstream winds) and the depth of the MBL. These factors are summarized using the conceptual model introduced in section 1 (Fig. 3). For cases with a strong large-scale pressure gradient and a deep MBL, the flow behaves much like a supercritical coastal flow. With supercritical flow, we expect coastal variations to create regions of acceleration and wind turning, depending on the orientation of the coastline and strength of the flow. The main effects are caused by the higher, inland Santa Ynez Mountains, which act as a barrier to the flow creating an expansion fan over the western SBC and a sheltered region with light winds over the coastal region south toward Los Angeles. Observations along the north shore of the SBC show that in most cases the sheltered region extends as a narrow band out to PC (see Fig. 1). However, the model is unable to reproduce this effect with 4-km resolution, creating the persistent offshore flow noted above.

When the MBL is shallow (~200 m) and wind speeds are reduced, the upstream flow becomes subcritical, leading to a transcritical situation for the SBC region (Fig. 3b). In this case, the interaction of the MBL with the coastline and Channel Islands forces a limited region of supercritical flow, covering most of the SBC and the Channel Islands. The flow characteristics in this case are very similar to idealized shallow water model results for transcritical flow (BHS; Rogerson 1999), showing an acceleration as the flow rounds PC into an expansion fan and then a rapid deceleration as the flow leaves the supercritical region.

Diurnal heating disrupts the flow pattern by changing the strength of the pressure gradient in the nearshore region. At night, an offshore pressure gradient is produced by cooling over the land, resulting in downslope flow off of the terrain. In the transcritical case, the downslope flow causes the formation of a gravity wave or internal bore disturbance in the eastern SBC that propagates westward, eventually reaching the Channel Islands and the western end of the SBC as shown schematically in Fig. 19. This propagation scenario is in agreement with trapped disturbance simulations for transcritical flow presented in Rogerson (1999). When the flow is supercritical, the effects of cooling are not as significant because the background flow is too strong for significant disturbance propagation. Instead, the cold air produced by nighttime cooling causes the sheltered region to shift slightly from the coastal region to the central SBC, with little effect on the winds over the western SBC.

Analysis of the horizontal momentum budget for the transcritical case shows the dominant role that the pres-

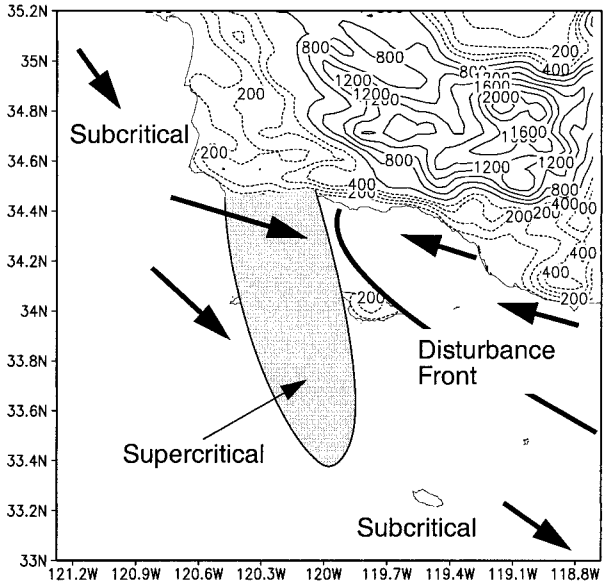

FIG. 19. Schematic showing how a gravity wave disturbance or bore propagates from inland regions westward across the SBC during transcritical flow conditions. As the disturbance propagates, the region of supercritical flow is reduced in size.

sure gradient term has in controlling the local wind direction and velocity. For alongshore winds, the momentum balance is mostly between the pressure gradient term and the ageostrophic acceleration produced by surface friction and nonlinear advection. Cross-shore flow is dominated by a balance between the pressure term and the surface friction. In general, the momentum budget shows that the flow behaves like a supercritical fluid over the entire SBC during the late afternoon and early evening hours when the onshore pressure gradient is enhanced by surface interior heating. At those times, the velocity field shows a strong acceleration in response to the local terrain-forced pressure gradient, consistent with supercritical flow dynamics (i.e., an expansion fan in the lee of PC). During the night and in the early morning, diurnal cooling modifies the nearshore boundary layer density and corresponding hydrostatic pressure, forcing offshore winds as the pressure increases over land. Changes in the MBL structure propagate across the SBC as an internal wave or bore (indicated by the disturbance front in Fig. 19), lifting the MBL and effectively eliminating the supercritical flow expansion fan in the lee of PC.

Overall, the simulations presented in this study give an optimistic outlook for forecasting coastal winds in areas of complex terrain using high-resolution mesoscale models. A key factor for success is ensuring that horizontal model resolution is appropriate for the local terrain features. For example, in our results, underresolving the rapid terrain increase along the northern shore lead to a persistent simulated offshore wind component that is rarely observed at surface stations. This affected the wind fields over the SBC, particularly at night when the offshore component was augmented by katabatic downslope winds. Other more minor differences were noted during periods of light and variable winds. Nevertheless, comparisons of the model with buoy observations shows that, at least over the water, resolving the coarse terrain features may be adequate in many cases. As computing resources become more economical, wind field simulations as presented here should become commonplace tools for the operational coastal forecaster.

Acknowledgments. We would like to thank Roger Samelson for helpful comments, George Taylor for ideas on possible case studies, and the very useful suggestions of the three anonymous reviewers. Profiler data used in this study were provided by the NOAA Environmental Technology Laboratory. This work was supported by the Office of Naval Research, Grant N00014-98-1-0113.

REFERENCES

Anderson, R. J., 1993: A study of wind stress and heat flux over the open ocean by the inertial-dissipation method. *J. Phys. Oceanogr.,* **23,** 2153–2161.

Atkinson, L. P., K. H. Brink, R. E. Davis, B. H. Jones, T. Paluszkiewicz, and D. W. Stuart, 1986: Mesoscale hydrographic variability in the vicinity of Point Conception and Arguello during April–May 1983: The OPUS 1983 Experiment. *J. Geophys. Res.,* **91** (C11), 12 899–12 918.

Bosart, L. F., 1983: Analysis of a California Catalina eddy event. *Mon. Wea. Rev.,* **111,** 1619–1633.

Brink, K. H., 1983: The near-surface dynamics of coastal upwelling. *Progress in Oceanography,* Vol. 12, Pergamon Press, 223–257.

Burk, S. D., T. Haack, and R. M. Samelson, 1999: Mesoscale simulation of supercritical, subcritical, and transcritical flow along coastal topography. *J. Atmos. Sci.,* **56,** 2780–2795.

Byun, D. W., 1990: On the analytical solutions of flux-profile relationships for the atmospheric surface layer. *J. Appl. Meteor.,* **29,** 652–657.

Caldwell, P. C., D. W. Stuart, and K. H. Brink, 1986: Mesoscale wind variability near Point Conception, California during spring 1983. *J. Climate Appl. Meteor.,* **25,** 1241–1254.

Clark, J. H. E., and S. R. Dembeck, 1991: The Catalina Eddy event of July 1987: A coastally trapped mesoscale response to synoptic forecasting. *Mon. Wea. Rev.,* **119,** 1714–1735.

Dorman, C. E., 1985: Evidence of Kelvin waves in California's marine layer and related eddy generation. *Mon. Wea. Rev.,* **113,** 827–839.

——, and C. D. Winant, 1995: Buoy observations of the atmosphere along the west coast of the United States, 1981–1990. *J. Geophys. Res.,* **100,** 16 029–16 044.

——, and ——, 2000: The structure and variability of the marine atmosphere around the Santa Barbara Channel. *Mon. Wea. Rev.,* **128,** 261–282.

——, D. P. Rogers, W. Nuss, and W. T. Thompson, 1999: Adjustment of the summer marine boundary layer around Pt. Sur, California. *Mon. Wea. Rev.,* **127,** 2143–2159.

——, T. Holt, D. P. Rogers, and K. Edwards, 2000: Large-scale structure of the June–July 1996 marine boundary layer along California and Oregon. *Mon. Wea. Rev.,* **128,** 1632–1652.

Eddington, L. W., 1985: A numerical simulation of a topographically forced wind maximum in a well-mixed marine layer. OPUS Tech. Rep. 16, FSU-MET-OPUS-85-1, 61 pp. [Available from Dept. of Meteorology, The Florida State University, Tallahassee, FL 32306.]

Harms, S., and C. D. Winant, 1998: Characteristic patterns of the

circulation in the Santa Barbara Channel. *J. Geophys. Res.*, **103,** 3041–3065.

Huyer, A., 1983: Coastal upwelling in the California current system. *Progress in Oceanography*, Vol. 12, Pergamon Press, 259–284.

Kidwell, K. B., Ed., 1990: *Global Vegetation Index User's Guide.* National Climatic Data Center, 45 pp.

Mass, C., and M. D. Albright, 1989: Origin of the Catalina eddy. *Mon. Wea. Rev.*, **117,** 2406–2436.

Rogerson, A. M., 1999: Transcritical flows in the coastal marine atmospheric boundary layer. *J. Atmos. Sci.,* **56,** 2761–2779.

Rosenthal, J., 1968: A Catalina eddy. *Mon. Wea. Rev.,* **96,** 742–743.

Samelson, R. M., 1992: Supercritical marine-layer flow along a smoothly varying coastline. *J. Atmos. Sci.,* **49,** 1571–1584.

——, and S. J. Lentz, 1994: The horizontal momentum balance in the marine atmospheric boundary layer during CODE-2. *J. Atmos. Sci.,* **51,** 3745–3757.

Sun, W.-H., and C.-Z. Chang, 1986: Diffusion model for a convective layer. Part I: Numerical simulation of convective boundary layer. *J. Climate Appl. Meteor.,* **25,** 1445–1453.

Troen, I., and L. Mahrt, 1986: A simple model of the atmospheric boundary layer: Sensitivity to surface evaporation. *Bound.-Layer Meteor.*, **37,** 129–148.

Wakimoto, R. M., 1987: The Catalina eddy and its effects on pollution over southern California. *Mon. Wea. Rev.*, **115,** 837–855.

Winant, C. D., C. E. Dorman, C. A. Friehe, and R. C. Beardsley, 1988: The marine layer off northern California: An example of supercritical channel flow. *J. Atmos. Sci.,* **45,** 3588–3605.

Xue, M., K. Droegemeier, V. Vong, A. Shapiro, and K. Brewster, 1995: APRS Version 3.0 User's Guide. Center for the Analysis and Prediction of Storms, University of Oklahoma, 380 pp. [Available from Center for the Analysis and Predication of Storms, University of Oklahoma, Norman, OK 73019.]